


**Please cite the Published Version**

Aliasghari, Sepideh, Hashimoto, Teruo, Kelly, Peter  and Matthews, Allan (2024) Synthesis of organic-inorganic 3D-nanocontainers for smart corrosion protection of friction stir welded AZ31B magnesium alloy-titanium dissimilar joints. *Journal of Magnesium and Alloys*, 12 (9). pp. 3589-3601. ISSN 2213-9567

**DOI:** <https://doi.org/10.1016/j.jma.2024.09.004>

**Publisher:** Elsevier/KeAi Communications Co., Ltd.

**Version:** Published Version

**Downloaded from:** <https://e-space.mmu.ac.uk/635589/>

**Usage rights:**  [Creative Commons: Attribution 4.0](https://creativecommons.org/licenses/by/4.0/)

**Additional Information:** This is an open access article which first appeared in *Journal of Magnesium and Alloys*

**Enquiries:**

If you have questions about this document, contact [openresearch@mmu.ac.uk](mailto:openresearch@mmu.ac.uk). Please include the URL of the record in e-space. If you believe that your, or a third party's rights have been compromised through this document please see our Take Down policy (available from <https://www.mmu.ac.uk/library/using-the-library/policies-and-guidelines>)



Full Length Article

# Synthesis of organic-inorganic 3D-nanocontainers for smart corrosion protection of friction stir welded AZ31B magnesium alloy-titanium dissimilar joints

Sepideh Aliasghari<sup>a,b,c,\*</sup>, Teruo Hashimoto<sup>b</sup>, Peter Kelly<sup>c</sup>, Allan Matthews<sup>a,b</sup>

<sup>a</sup>Henry Royce Institute, Department of Materials, The University of Manchester, Manchester, M13 9PL, UK

<sup>b</sup>Department of Materials, The University of Manchester, Manchester, M13 9PL, UK

<sup>c</sup>Surface Engineering Group, Department of Engineering, Manchester Metropolitan University, Manchester, M1 5GD, UK

Received 18 July 2024; received in revised form 6 September 2024; accepted 9 September 2024

Available online 25 September 2024

## Abstract

The joining of different light metals through friction stir welding (FSW) is gaining interest as a method to decrease weight and improve fuel efficiency. However, to ensure durability, these welded metals may require surface treatments to protect against corrosion or wear. This study presents a novel approach for the simultaneous delivery of two distinct corrosion inhibitors to Ti-Mg dissimilar PEO treated joints on demand. The research focuses on the synthesis, characterization, and application of cerium@polystyrene (Ce@PS) nanocontainers, which are loaded with 8-hydroxyquinoline (8-HQ) to enhance corrosion protection. The synthesis involves several key steps, including the formation of a cerium-based outer layer around polystyrene nanospheres, the selective removal of the polystyrene core to create a porous structure, and the subsequent loading of the 8-HQ inhibitor. Structural and compositional analyses, conducted using scanning transmission electron microscopy (STEM) and energy-dispersive X-ray spectroscopy (EDS), confirmed the successful incorporation of 8-HQ within the nanocontainers. Additionally, Fourier-transform infrared spectroscopy (FTIR) provided detailed information about the chemical composition of the organic materials throughout the synthesis process. Thermal decomposition analysis verified the successful fabrication and stability of the dual-shell nanocontainers.

Corrosion tests on Ti-Mg joints treated with plasma electrolytic oxidation (PEO) coatings and loaded nanocontainers demonstrated significantly improved corrosion resistance compared to untreated joints. This research highlights the potential of dual-shell nanocontainers, containing both organic and inorganic inhibitors, to offer prolonged corrosion protection, particularly against galvanic corrosion in dissimilar joints. The findings suggest that these synthesized nanocontainers hold promise for various industrial applications, particularly in the context of friction stir welded (FSW) Ti-Mg dissimilar joints, providing valuable insights for the development of advanced materials designed to mitigate corrosion.

© 2024 Chongqing University. Publishing services provided by Elsevier B.V. on behalf of KeAi Communications Co. Ltd.

This is an open access article under the CC BY-NC-ND license (<http://creativecommons.org/licenses/by-nc-nd/4.0/>)

Peer review under responsibility of Chongqing University

**Keywords:** AZ31B; Magnesium; Dissimilar joint; Two-shell inhibitors; Smart corrosion protection.

## 1. Introduction

Titanium (Ti) and magnesium (Mg) are commonly used in the automotive and aerospace industries to reduce the weight of components. Optimizing a design may require joining these metals, with friction stir welding (FSW) being a candidate

method. FSW is a solid-state process involving frictional heat from a rotating pin and intense plastic deformation of the metals leading to fine equiaxial recrystallized grains [1,2]. Since dissimilar metal joints can be sites of corrosion due to variations in chemistry, microstructure and residual stress [3], a surface treatment for corrosion protection may be needed.

Plasma electrolytic oxidation (PEO), an environmentally sustainable surface treatment, is applicable to both Mg and Ti. The resultant coatings have been extensively studied. High-

\* Corresponding author.

E-mail address: [Sepideh.Aliasghari@manchester.ac.uk](mailto:Sepideh.Aliasghari@manchester.ac.uk) (S. Aliasghari).

voltage electrolysis, often using alkaline electrolytes, causes microdischarges on the substrate that stimulate oxidation, thermal, and plasma-driven reactions, resulting in corrosion- and wear-resistant coatings [4–7]. The PEO coatings contain an inner, adherent, compact layer and an outer porous layer that offers flexibility of thickness [8].

The pores result mainly from H<sub>2</sub>, O<sub>2</sub>, and H<sub>2</sub>O vapour generated during PEO [9] and allow a functionalizing post-treatment, such as loading a corrosion inhibitor [10,11]; e.g. 8-hydroxyquinoline (8-HQ) [12,13], cerium ions [14,15]; layered double hydroxide (LDH) loaded with molybdate [16] and halloysite nanotubes (HNTs) loaded with vanadate, molybdate and 8-HQ [17,18] have been added to PEO-coated Mg alloys.

Incorporating inhibitor in nanocontainers can be used to create a self-healing coating that may reduce the costs of corrosion. The inhibitors are released by triggers such as pH change, ion exchange, mechanical, chemical, or thermal damage, electric fields and oxidation reduction reactions [19,20]. The shell regulates the release kinetics, which can be either irreversible or reversible based on whether there is complete rupture or permeability. Polymer shells have often been employed, either independently or with other components, [21,22] eg polyurethane, polystyrene, polyacrylate, melamine resins, siloxanes, and sulfones [23–27]. Shells can be created through solvent evaporation and then incorporated into epoxy resin. Chemical and physical methods exist for microencapsulation. Chemical polymerization encompasses techniques like suspension, dispersion, and poly-condensation that forms a solid layer around the active core [28]. Physical methods include layer-by-layer (LbL) assembly, sol–gel, CO<sub>2</sub>-assisted microencapsulation, or physicochemical methods like spray drying, vacuum encapsulation, multiple nozzle spraying, electrostatic encapsulation, fluid-bed coating, and centrifugal techniques [29–32]. Alternatively, inhibitors can be encapsulated using nanocontainers formed from LbL silica or mesoporous silica (SiNC) [33–35], ZnO [36], LDHs [37], TiO<sub>2</sub> [38] and HNTs [39].

The size and loading capacity of nanocontainers are important for the performance of the coating. The nanocontainers should also be chemically compatible with the coating, exhibit strong adhesion to it [40], and neither prematurely rupture nor fail to release contents on demand. Combinations of hydrophilic and hydrophobic shell layers, possibly with the addition of a second or third layer, have been considered [41,42]. Studies have suggested that a low inhibitor concentration in small-sized containers may enhance the coating toughness [43], while larger containers may provide better protection at the same weight [40]. A main challenge remaining is to load inhibitors in precise quantities that guarantee repair of defects.

The current project examined the formation of a two-shell nanocontainer, namely Ce@PS. The outer cerium-rich shell serves as a reservoir of inorganic inhibitor. The inner shell, derived from a polystyrene (PS) template, contains 8-HQ, which can be released into aqueous solutions. Thus two inhibitors are available for different corrosion scenarios. The morphology and composition of the nanocontainers were characterized

using scanning transmission electron microscopy (STEM), scanning electron microscopy (SEM), Fourier transform infrared (FT-IR) spectroscopy and thermogravimetric analysis (TGA). The nanocontainers were added to an epoxy layer above PEO coatings on FSW AZ31B /Ti joints and corrosion protection evaluated in NaCl solution. Information on PEO of paired metals is limited. Coatings similar to those of the metals treated individually were found on Al/AA7075 and AA7075/ZE41 pairs [44] and a thicker coating at the joint lines of AlMgSi1-clad/Mg(AZ31)-core alloy [45]. Of present relevance, although PEO prevented general corrosion of the Mg-side of FSW Ti-AZ31 joints, localized corrosion occurred [46].

## 2. Materials and methods

### 2.1. Materials and reagents

PS latex microspheres with a size of 0.50 μm from Alfa Aesar and ammonia (20%, aqueous solution), acetonitrile, cerium acetylacetonate (Ce(acac)<sub>3</sub>), epoxy resin based on Phenol 4,40 -(1-methylethylidene) bis- Araldite GY 257', G GY 257, 2,2'-diaminodiethylamine, sodium chloride, sodium hydroxide pellets, and absolute acetone (ACS grades) were purchased from Sigma Aldrich and used in as-received condition without further purification.

For the fabrication of joints, sheets measuring 50 × 150 × 2 mm were used. These sheets were composed of materials with high purity, specifically AZ31B magnesium alloy (comprising Al 2.5–3.5%, Zn 0.7–1.3%, Mn 0.2–1.0%, and Mg as the balance), and commercial purity titanium (99.6% purity). The joints were created using the Friction Stir Welding (FSW) process, both with and without prior Plasma Electrolytic Oxidation (PEO) treatment. This approach aligns with the methodology established in previous reports authored by the researchers [46].

### 2.2. Synthesis of Ce@PS nanocontainers loaded with 8-hydroxyquinoline (8-HQ) organic corrosion inhibitor

The polystyrene (PS) nanospheres were utilized as templates for creating the Ce component outer layer. The synthesis of the outer shell composed of cerium was achieved through the sol–gel method, involving the following steps: initially, 0.1 g of PS nanospheres were placed in a three-headed round bottom flask. Subsequently, 40 ml of acetonitrile was added to the flask. The temperature was carefully maintained at 75 °C by introducing 1 ml of ammonia and 0.1 g of cerium acetylacetonate into the mixture. After allowing the reaction to proceed for 18 h at 75 °C, Ce@PS core–shell nanospheres were formed. These core–shell nanospheres were then purified by subjecting them to three rounds of centrifugation in acetonitrile, effectively removing any unreacted cerium acetylacetonate. The selective removal of the PS template was achieved by immersing the Ce@PS nanospheres in an acetone solution. To load the corrosion inhibitor into

the nanocontainers, a vacuum-induced capillarity method was employed.

Saturated aqueous solutions of 8-hydroxyquinoline (8-HQ) were mixed with the Ce@PS nanospheres.

The suspension was placed in a beaker and maintained at 22 °C with continuous agitation. A vacuum pump was utilized to evacuate the air from the suspension, and this process was sustained for 20 min. This vacuum-induced capillarity process was repeated three times to ensure maximum loading of the corrosion inhibitor. Finally, the loaded nanospheres were washed with ethanol and dried at room temperature.

### 2.3. Post treatment: epoxy topcoat PEO treated FSW Mg alloy-Ti joint

The process of incorporating organic inhibitor-loaded two-shell containers into PEO coatings involved post-treatment through immersion in epoxy resin and proceeded as follows: initially, 3 wt.% of Ce@PS loaded with the 8-Hydroxyquinoline (8-HQ) organic inhibitor was added to the epoxy resin. The resulting mixture was subjected to mechanical stirring for 15 min. Subsequently, the hardener was introduced into the mixture at a ratio of 10:1 (wt.%). After two minutes of agitation, the epoxy coatings were applied to the PEO joint specimens using the dip-coating method. During the dip-coating process, the specimens were immersed in the resin for 30 s and then withdrawn at a speed of 20 cm per minute. This dipping process was repeated three times. Following the coating application, the joint specimens were left to dry at room temperature for a period of 72 h [47].

### 2.4. Characterization

Attenuated Total Reflection Fourier Transform Infrared Spectroscopy (ATR FTIR) was employed for spectral analysis. The following procedure was followed: background spectra were initially collected to provide a baseline reference. Spectra for polystyrene (PS), 8-Hydroxyquinoline (8-HQ), and two-shell Ce@PS nanospheres, both with and without 8-HQ as the organic inhibitor, were recorded in transmittance mode. A Nicolet 5700 FTIR spectrophotometer was utilized to acquire these transmittance spectra within the wavelength range of 500 to 4000  $\text{cm}^{-1}$ . The collection of infrared spectra was performed in reflectance mode with 16 accumulations with a spectral resolution of 4  $\text{cm}^{-1}$ .

A ZEISS Sigma VP FEG-SEM instrument was employed for SEM analysis. It operated at a voltage of 1 kV under low vacuum conditions suitable for studying polymers. This technique allowed for the examination of the morphology of polystyrene and the two-shell Ce@PS nanocontainers, both without and with the 8-HQ. The structure and elemental composition of the Ce@PS nanocontainers were investigated using a FEI Titan G2 80–200 Chemistem transmission electron microscope. This TEM was equipped with four silicon-drift EDS detectors, an in situ objective lens, and operated at an acceleration voltage of 200 kV. Micrographs were obtained using scanning transmission electron microscopy (STEM) with

a high-angle annular dark-field (HAADF) detector. To prepare the samples, a holey carbon TEM grid was immersed in a solution containing 1 mg of nanocontainers dispersed in 50 ml of acetonitrile and then dried at room temperature.

Thermogravimetric (TGA) measurements were performed using a TA Instruments Q500 TGA, at the heating rate of 10°C/min in argon from 20 °C to 500 °C.

The UV–Vis spectroscopy analysis of the release of an inorganic cerium compound from the two-shell nanocontainer was conducted using a PerkinElmer Lambda 35 spectrophotometer, operating at a medium performance level, within the spectral range of 200–450 nm. A calibration curve for cerium was constructed using cerium nitrate solutions at concentrations of 0.00006, 0.00004, 0.0009, and 0.005 mol/l dissolved in water at pH 6.5. The absorption peaks at a wavelength of  $\lambda = 252$  nm for cerium were utilized within the investigated range. 3.25 g of two-shell material were dispersed into a 50 ml volume flask of deionized water under stirring conditions at 150 rpm. Subsequently, at specific time intervals, 2 ml samples were withdrawn from the dispersion and filtered for analysis. Following measurement, all the sampled volumes were returned to the original flask.

### 2.5. Corrosion resistance evaluation

The corrosion resistance of the bare Ti and Mg, joint with-out and with PEO and following epoxy resin impregnation containing two shell nanocontainers were evaluated using immersion and electrochemical techniques in a naturally aerated aqueous solution of 3.5 wt% NaCl at 23 °C and pH = 6.5. A Solartron Modulab computer-controlled potentiostat connected to a three-electrode electrochemical cell was used. The material tested at the joint acted as a working electrode (1  $\text{cm}^2$ ), whereas a platinum plate and a silver/silver chloride (Ag/AgCl, 3 M KCl, 0.210 V vs SHE) electrode were considered as the counter and reference electrodes, respectively. The potential sweep was acquired from  $-1.5$  V to  $+1$  V versus the open circuit potential (OCP) at a scan rate of 0.2 mV  $\text{s}^{-1}$ .

In the immersion test, Ti-Mg welds with PEO coatings were immersed in 100 ml of 3.5 wt% NaCl solution at room temperature ( $\sim 20$  °C). The specimens, with PEO coating thicknesses of 4–12  $\mu\text{m}$  on the Mg side and 5–18  $\mu\text{m}$  on the Ti side, were coated without or with epoxy containing inhibitor-loaded nanocontainers. A 20 mm scratch was made across the welds, with half on the Mg side and half on the Ti side. The samples were then immersed for different hours.

## 3. Results

### 3.1. Synthesis and characterization of Ce@PS nanocontainers loaded with 8-hydroxyquinoline (8-HQ)

Fig. 1 shows a schematic of the synthesis of Ce@PS loaded with organic 8-HQ inhibitor formed in four stages.

In stage (A), an outer layer of cerium compound was created around the initially received polystyrene nanospheres.

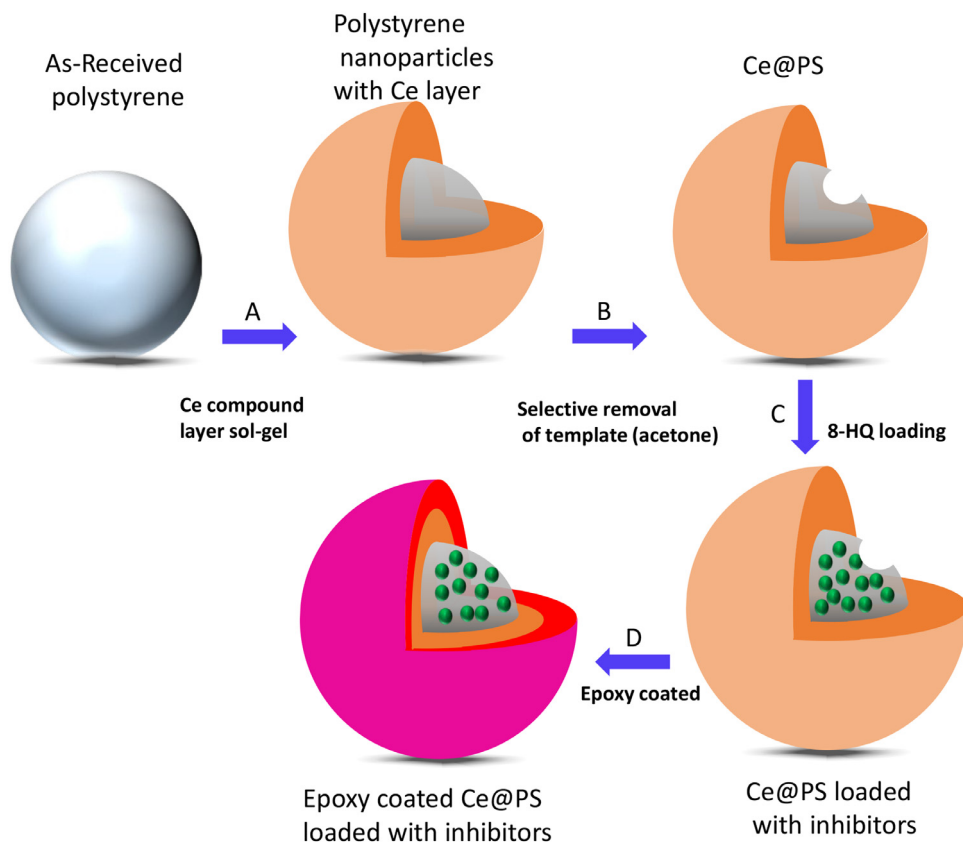


Fig. 1. Schematic formation of epoxy coated two shell polystyrene nanocontainers loaded with 8-HQ in four stages (A, B, C, D).

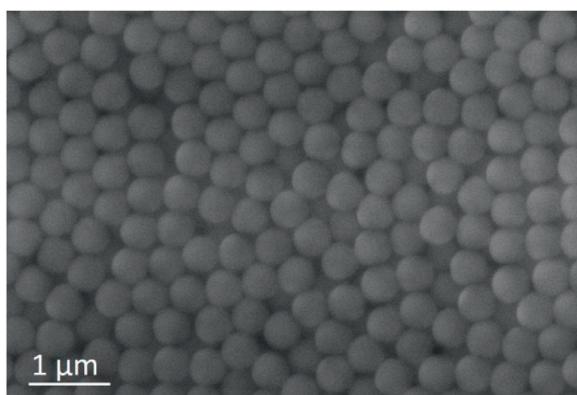


Fig. 2. SEM Secondary electron images of as-received polystyrene nanospheres.

This was achieved through a sol-gel immersion process in cerium acetylacetonate, conducted at 75°C for 18 h. Fig. 2 displays a scanning electron micrograph of the polystyrene particles in their dried emulsion state. These particles exhibit a size distribution falling within the range of 400 to 450 nm and possess a surface that is both smooth and uniform.

Fig. 3 revealed EDS elemental maps of a scanning electron micrograph of carbon, cerium and oxygen after the sol-gel process, stage (A). The EDS map shows the homogenous carbon rich distribution within the inner part of the spheres, which is related to the presence of the PS polymer. Cerium-rich regions of up to a few tens nanometres in size in the

outer region of the carbon nanoparticles are evident. Oxygen is relatively uniformly distributed, with a slight enrichment on the outer layer.

Following this, in stage (B), acetone was added to the mixture to selectively remove the PS template by partially dissolving it. Fig. 4 clearly reveals the removal of the polystyrene from the inner part of the nanoparticles, resulting in a porous structure enriched in cerium in the outer region. The presence of porosity and voids resulting from the selective removal process will serve to provide reservoirs for the incorporation of corrosion inhibitors.

In step (C), 8-HQ corrosion inhibitor was loaded under vacuum condition to the porous structure of Ce@PS.

HAADF transmission electron micrographs of Ce@PS nanocontainers loaded with 8-HQ at the final stage are shown in Fig. 5(a). An increased magnification image of a loaded nanocontainer marked as (A) present in Figs. 5 (b, c) shows details of the inset region of Fig. 5(a). The HAADF image reveals regions of different contrast that result from differences in the composition and/or different thickness of the Ce@PS. The nanocontainers have a spherical shape, typically with sizes up to 450 nm in diameter. EDS areas of elemental mapping (Fig. 4d-f) indicate that the nanocontainers contains oxygen, cerium and carbon. Cerium was concentrated around the peripheries of the polymer with smaller amounts in the main body of the inner shell. Mapping of cerium and oxygen reveals the presence of cerium, likely in the form of oxide, in the outer thin region with a thickness of 15–20 nm. The in-



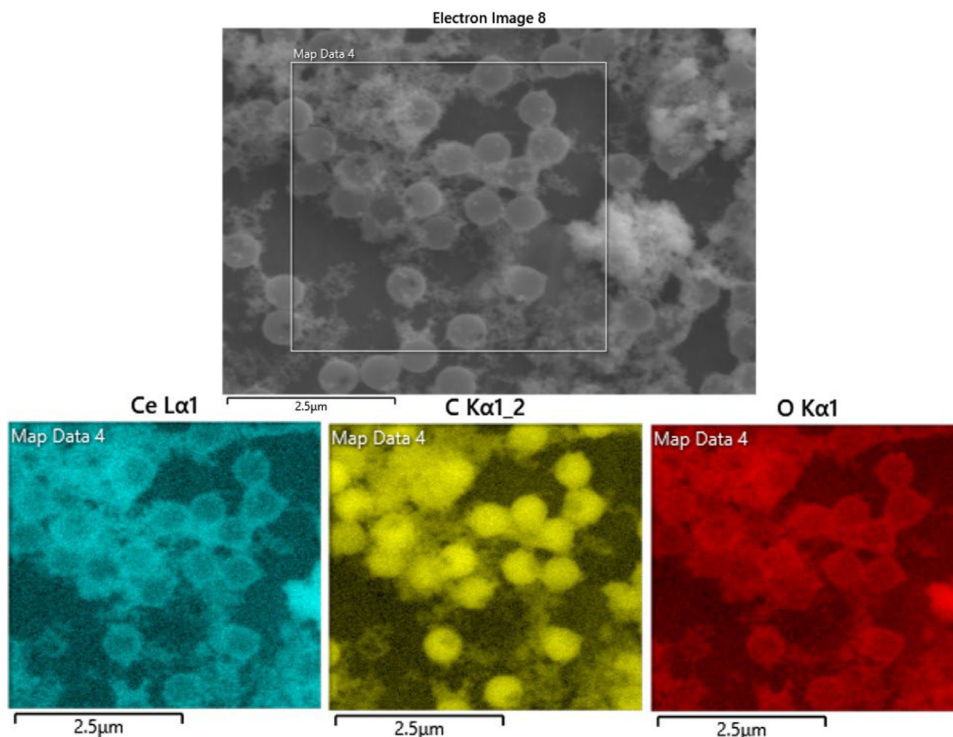


Fig. 3. EDS elemental maps of a scanning electron micrograph (secondary electrons) of cerium, carbon and oxygen in stage (A).

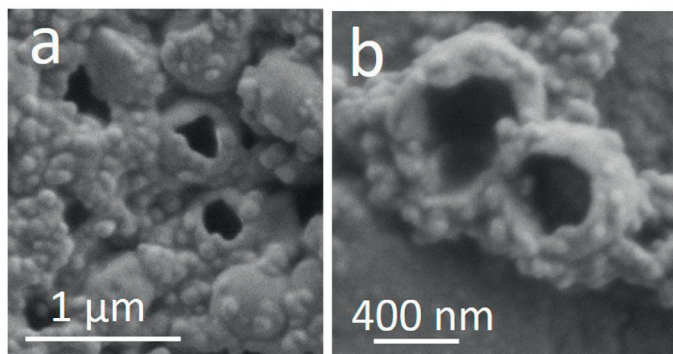


Fig. 4. Scanning electron micrograph (secondary electrons) of Ce@PS in stage (B), showing the presence of porosity and voids.

ner region of Ce@PS is clearly enriched in carbon, the main forming element of 8-HQ, confirming its successful incorporation, although residual carbon from the polymer template may also be present.

Table 1, shows the normalized percent of the elemental concentration in corresponding areas from EDS mapping of TEM micrographs of 8-HQ loaded Ce@PS nanocontainers presents in Fig. 5(b).

### 3.2. Structural and compositional analysis

Fig. 6 shows the FTIR spectra of the as received polystyrene polymer, as received cerium acetylacetonate ( $\text{Ce}(\text{acac})_3\text{H}_2\text{O}$ ), polystyrene with cerium component in the outer shell before immersion in acetone, as received 8-HQ, two shell without 8-HQ and two shell nanocontainer loaded with 8-HQ. Peaks at 696, 749, 1452, 1490  $\text{cm}^{-1}$  reveal well-

defined bands of the phenyl group in PS. Fig. 6 also reveals specific absorption bands at 696, 749  $\text{cm}^{-1}$  associated with CH out-of-the plane vibrations; 1028  $\text{cm}^{-1}$  ascribed to  $\text{CH}_2$  ring plane; 1452  $\text{cm}^{-1}$  related to H–C–H chain ending, 1490  $\text{cm}^{-1}$  for C–C ring stretching, 2926  $\text{cm}^{-1}$  associated with  $\text{CH}_2$  symmetric and asymmetric chain stretching and 3026  $\text{cm}^{-1}$  assigned to C–H ring stretching [48]. The released components of the nanospheres were identified mostly on the basis of their FTIR reference spectra available on the world-wide web in the public domain spectral libraries of NIST [49]. The cerium acetoacetanate ( $\text{Ce}(\text{acac})_3\text{H}_2\text{O}$ ) shows  $\text{Ce}(\text{OH})^{2+}$  in the regions of 500–750  $\text{cm}^{-1}$  [50], specific peaks at 1571, 1511 1511, and 1380  $\text{cm}^{-1}$ , which are associated with vibration bonds in C=O; antisymmetric vibration of C=C and stretching for  $\text{CH}_3$ , respectively. The 1255  $\text{cm}^{-1}$  is associated with vibration of C=C bonds; 1016  $\text{cm}^{-1}$  vibration of C–C; 920  $\text{cm}^{-1}$  vibration of C– $\text{CH}_3$ , and the broad peaks in the range of 3197–3450 correspond to the O–H stretching band of water [50–52]. The polystyrene and cerium compound in the outer layer without removing the polystyrene template (stage A) shows peaks of polystyrene and cerium acetylacetonate. Peaks at 2252  $\text{cm}^{-1}$  and 2292  $\text{cm}^{-1}$  present a triple bond of carbon with nitride from acetonitrile as a solvent during the formation of the cerium oxide top shell. 8-HQ, with chemical formula  $\text{C}_9\text{H}_7\text{NO}$ , has two identified OH and NH groups in its structure. The FTIR spectrum shows a wide band at 3000  $\text{cm}^{-1}$ , which is associated with the N–H stretching vibration band of the NH group of the ring [53]. The bands located in the range 1164–1578  $\text{cm}^{-1}$  are related to C–N ring stretching vibrations, in-plane O–H bending, O–H deformation, and C–O stretching [54,55] and the bands located

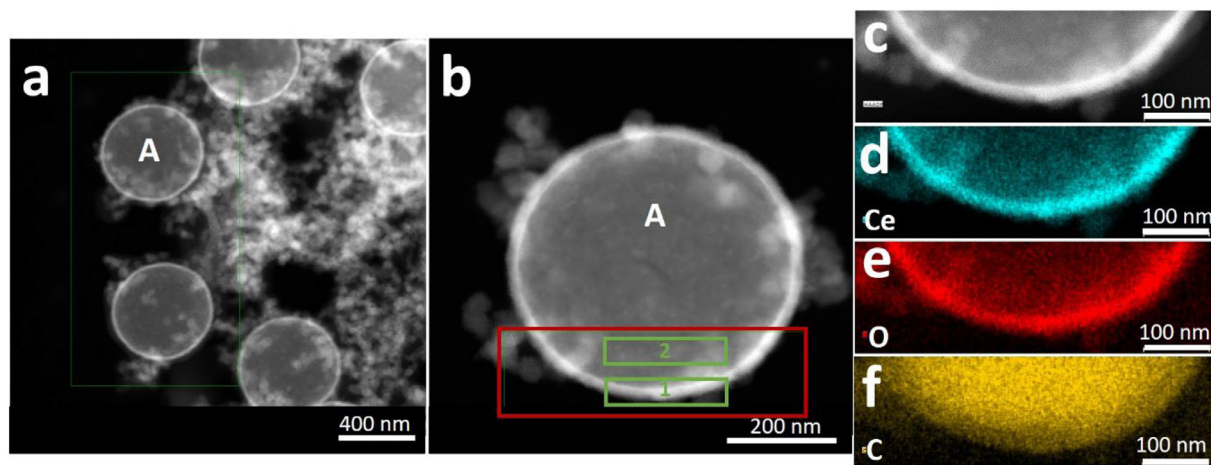


Fig. 5. (a) Transmission electron micrographs, (b) increased magnification from (a) micrographs, (c) EDS mapping, (d) cerium, (e) oxygen and (f) carbon of Ce@PS loaded with 8-HQ in stage (C).

Table 1

EDS concentration of inset regions 1 and 2 from of 8-HQ loaded Ce@PS nanocontainers shown in Fig. 5b.

| Regions (at.%) | Cerium | Carbon | Oxygen |
|----------------|--------|--------|--------|
| Area 1         | 2.3    | 67.1   | 30.6   |
| Area 2         | 0.3    | 89.9   | 9.8    |

between 500–700  $\text{cm}^{-1}$  are associated with O–H stretching bonds [56]. Two shells without 8-HQ shows well-defined peak of PS assigned at 700 and 750  $\text{cm}^{-1}$  following peaks at 1450 to 1560  $\text{cm}^{-1}$  from the cerium compound. FTIR spectra of Ce@PS nanocontainers loaded with 8-HQ reveal clear peaks at 2981 and 2300  $\text{cm}^{-1}$  (marked with a circle symbol in Fig. 6), which are associated with N–H stretching of the NH group and C–H stretching vibrations of the ring, respectively [53]. Characteristic peaks of the cerium component are observed at 1379 and 1637  $\text{cm}^{-1}$ , which indicates that cerium with possible oxygen bonds were successfully formed [57].

Peaks at 1046  $\text{cm}^{-1}$  and 1091  $\text{cm}^{-1}$  identified the presence of a CH stretching band in the OH ring and N ring, respectively [54], while 879  $\text{cm}^{-1}$  shows a stretch band of C–OH (marked with a rectangular symbol in Fig. 6) [54], which suggest that 8-HQ has been successfully loaded in Ce@PS nanocontainers and two shell nanocontainers with outer inorganic and inner organic inhibitors formed.

The thermal decomposition behaviour, TgA diagrams, of polystyrene emulsion, pure 8-HQ and cerium compound ( $\text{C}_{15}\text{H}_{21}\text{CeO}_6 \cdot \text{H}_2\text{O} / \text{Ce}(\text{acac})_3 \cdot \text{H}_2\text{O}$ ) over the range of 20–500  $^\circ\text{C}$  is shown in Figure S1 and reveals several key findings. The polystyrene emulsion loses water at 87–98  $^\circ\text{C}$ , with polymer degradation starting at 404  $^\circ\text{C}$ , leaving no residue. While pure 8-HQ degrades between 155 and 167  $^\circ\text{C}$  without leaving residue. The cerium compound ( $\text{Ce}(\text{acac})_3 \cdot \text{H}_2\text{O}$ ) undergoes a multi-stage decomposition, with water loss at 107–141  $^\circ\text{C}$  and chelate ligand degradation between 269 and 434  $^\circ\text{C}$ , leaving approximately 50% residue corresponding to Ce IV. The presence of 8-HQ alters the TGA profile, with initial water loss at 92–107  $^\circ\text{C}$ , 8-HQ decomposition at 108–255  $^\circ\text{C}$ , and cerium

compound decomposition overlapping with polystyrene degradation at 272–407  $^\circ\text{C}$ . The incorporation of 8-HQ leads to a reduced cerium concentration, suggesting that the interaction between 8-HQ and cerium may affect the integrity of the cerium shell.

Release kinetics of the cerium inhibitor loaded in the nanocontainers using UV–vis spectrometry at 252 nm wavelength are shown in Figure S3. Approximately 90% of the cerium ( $\text{Ce}^{3+}$ ) was released within the first hour, indicating a rapid release phase that suggests the nanocontainers exhibit high initial burst release kinetics. The concentration of  $\text{Ce}^{3+}$  in the solution started within the first hour, reaching chemical ion-exchange equilibrium. This indicates that the release process is controlled and primarily governed by diffusion or dissolution mechanisms.

### 3.3. Corrosion evaluation of Ti–Mg joint without and with PEO and epoxy coated

The corrosion behaviour of the treated Ti–Mg joint immersed in 3.5 wt.% NaCl solution was studied by polarization and immersion measurements. Fig. 7 shows scanning electron micrographs of a PEO-coated friction stir welded (FSW) AZ31B alloy–titanium joint. Fig. 7(a) reveals the surface view, while Fig. 7(b) displays the cross-section. The upper and lower halves of the micrographs correspond to the coatings above the AZ31B alloy and titanium parts of the joint, respectively. No transitional interfacial region was observed, indicating a distinct compositional boundary between the AZ31B alloy and titanium, as evidenced in the cross-sectional images. The coating on the titanium exhibits a coarser texture compared to the coating on the AZ31B alloy, with a wide range of pore sizes. In contrast, the AZ31B alloy coating has finer pores, and lacks the nodular deposits observed on the titanium coating surface. The cross-section of the titanium side appears lighter due to increased electron scattering from titanium compared to the AZ31B alloy. The weld interface appears irregular due to severe deformation caused by

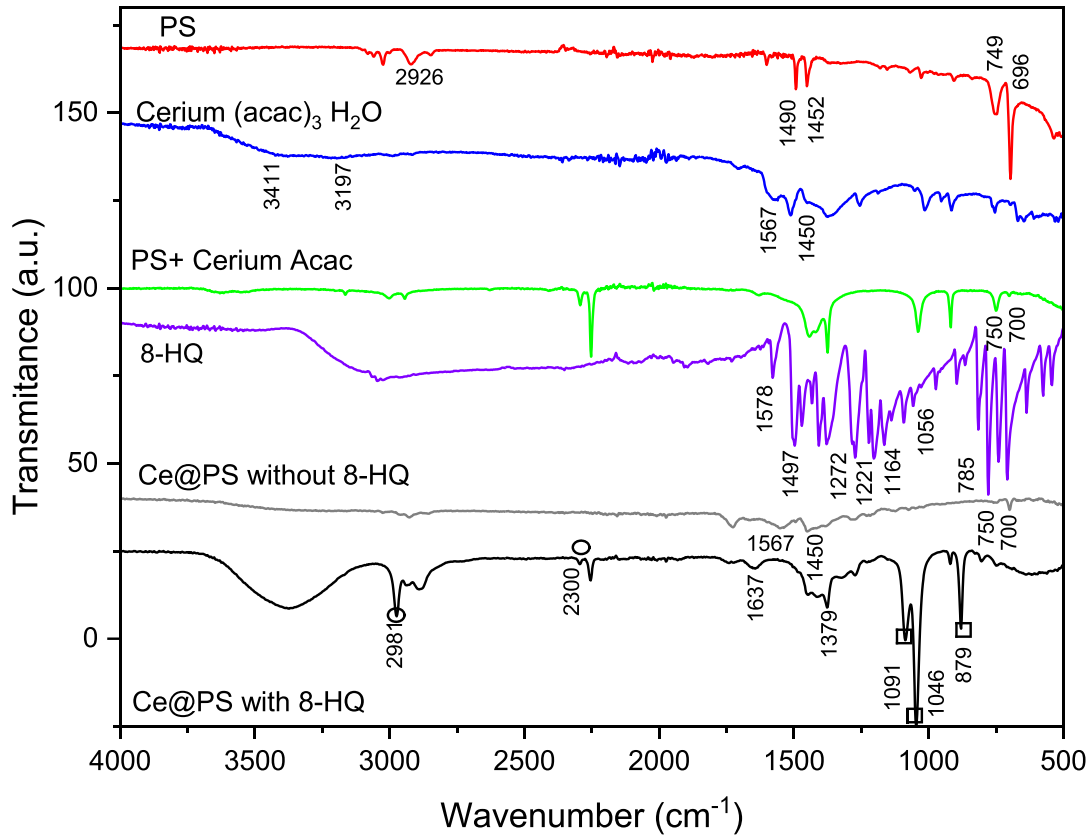


Fig. 6. ATR FTIR spectra of as received polystyrene polymer, as received cerium acetylacetonate ( $\text{Ce}(\text{acac})_3 \cdot \text{H}_2\text{O}$ ), as received 8-HQ, polystyrene (PS) with cerium oxide shell in outer layer without 8-HQ and two shell nanocontainer loaded with 8-HQ.

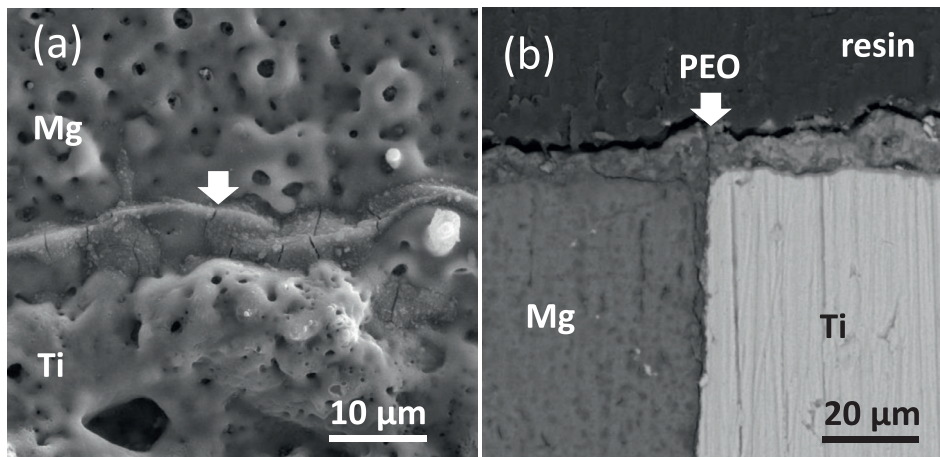


Fig. 7. (a) Scanning electron micrograph (secondary electrons) of the surface, (b) backscattered electron of the cross-section of an FSW AZ31B alloy-titanium joint following DC PEO at  $200 \text{ mA cm}^{-2}$  for 10 min in an alkaline silicate-based electrolyte.

the offset screw-type probe used in the friction stir welding process. The PEO process has resulted in porous coatings approximately  $4\text{--}12 \mu\text{m}$  thick on the AZ31B alloy and  $5\text{--}18 \mu\text{m}$  thick on the titanium, with average thicknesses around  $6 \mu\text{m}$  and  $10 \mu\text{m}$ , respectively.

Fig. 8 presents the potentiodynamic polarization curves of Ti and Mg bare material and joints without and with PEO coatings following being loaded with two shell nanocontainers

incorporating 8-HQ organic inhibitor with epoxy resin as a top coat. For all Ti-Mg joints, the corrosion potential ( $E_{\text{corr}}$ ) lies about between  $-0.59$  and  $-1.45 \text{ V Ag/AgCl}$ , which is the corrosion potential for bare titanium and magnesium, respectively. In the case of bare Ti-Mg joints, the corrosion potential is  $-1.47 \text{ V}$ , which is about  $-0.02 \text{ V}$  less than the corrosion potential of bare magnesium without any joint and the corrosion current density is lower than bare magnesium without a



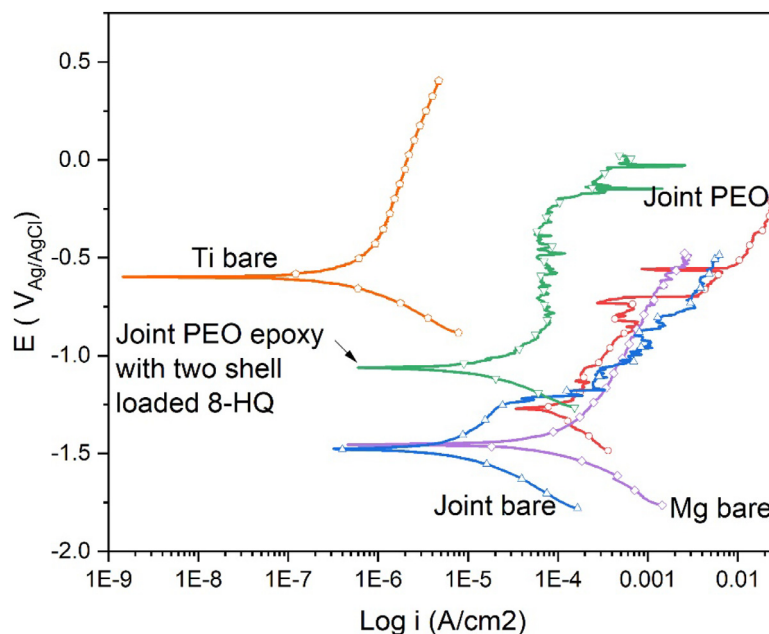


Fig. 8. Potentiodynamic polarization curves of the studied joints without and with PEO coated with two shell nanocontainer after 1 hour of immersion in naturally aerated 3.5% NaCl solution.

Table 2

Corrosion parameters calculated from the potentiodynamic polarization measurements.

| Specimen      | $E_{\text{corr}}$ (V<br>Ag/AgCl) | $i_{\text{corr}}$<br>(A/cm <sup>2</sup> ) | $\beta_{\text{c}}$<br>(V/dec) | $\beta_{\text{a}}$ (V/dec) |
|---------------|----------------------------------|---|-------------------------------|----------------------------|
| Bare Mg       | -1.45                            |   | -0.31                         | 0.38                       |
| Bare Ti       | -0.59                            | $9.04 \times 10^{-5}$                     | -0.32                         | 1.29                       |
| Bare joint    | -1.47                            | $4.77 \times 10^{-7}$                     | -0.23                         | 0.45                       |
| PEO joint     | -1.27                            | $8.25 \times 10^{-6}$                     | -0.39                         | 0.63                       |
| PEO joint     | -1.06                            | $1.10 \times 10^{-4}$                     | -0.18                         | 0.61                       |
| Ce@PS-<br>8HQ |                                  | $2.25 \times 10^{-5}$                     |                               |                            |

joint (Table 2). This is possibly attributed to galvanic interaction between the joint. While PEO-coated joints indicate an increase in potential from  $-1.47$  to  $-1.27$  V indicating the capacity of the barrier layer formed using the PEO method to protect the surface and improve corrosion behaviour [55]. However, a slight increase in current density was observed in comparison to the uncoated joint which could be explained by an increase in the specific surface area after PEO coating [17]. The PEO joint containing corrosion inhibitors (8-HQ) shows that the corrosion potential increased to  $-1.06$  V (Table 2) suggesting that the 8-HQ containing two shell nanocontainer has an influence on the corrosion resistance. This inhibition of corrosion action denotes that the combination of the epoxy polymer layer including loaded nanocontainers together with 8-HQ increased the corrosion protective properties. This improves the barrier properties of the coating due to preventing access of the electrolyte to the substrate and possibly insoluble complexes physically blocking the porosity of the PEO coated joint [56]. This kind of behaviour is commonly observed in thin films subjected to sealing post-treatment [58]. The epoxy coating loaded with inhibitor provides a region with anodic passivity and a slight reduction in the corrosion

current density compared to PEO coated joints. The integrity of a barrier oxide layer  $\lesssim 1$   $\mu\text{m}$  thick at the substrate that is formed usually by the PEO method provides barrier protection on the magnesium and the joint [59]. The porous outer layer slows down the transport of components between the bulk solution and metal that may assist with corrosion protection. The inevitable presence of defects in the FSW process for joining Mg to Ti may impair the integrity of the barrier layer so that the electrolyte can access the substrate easily and initiate corrosion.

The corrosion protection from two Ti-Mg welds was investigated, with a PEO coating of thickness 4–12  $\mu\text{m}$  on the Mg side and 5–18  $\mu\text{m}$  on the Ti side immersed in 3.5% NaCl. One weld had an epoxy top-coating applied and the other weld had an epoxy coating containing inhibitor-loaded nanocontainers applied. The epoxy layers were of similar thickness,  $\approx 75$   $\mu\text{m}$ . The specimens were scratched with a scalpel along a length of 20 mm with 50% in the Ti side and 50% on the Mg side. The edges and backs of the specimens were masked with lacquer. The specimens were then immersed in a beaker containing 100 ml of 3.5 wt% NaCl solution at room temperature, about 20 °C. After 100 h immersion, a small region of corrosion was observed on the Mg side of the scratch on the nanocontainer-free specimen (Fig. 9a). This increased in area to  $\approx 1$   $\text{mm}^2$  with increase of the test time to 272 h (Fig. 9c). No corrosion was evident on the specimen with nanocontainers (Fig. 9(b, d)). The limited extent of corrosion on the former specimen was considered to be due to expansion of the epoxy caused by absorption of water from the test solution that blocked access of the solution to the scratch surface [60]. Therefore, the specimens were re-scratched and re-immersed for 78 h in the same test original solution. Relatively severe corrosion occurred on the specimen without nanocontainers that had spread from the

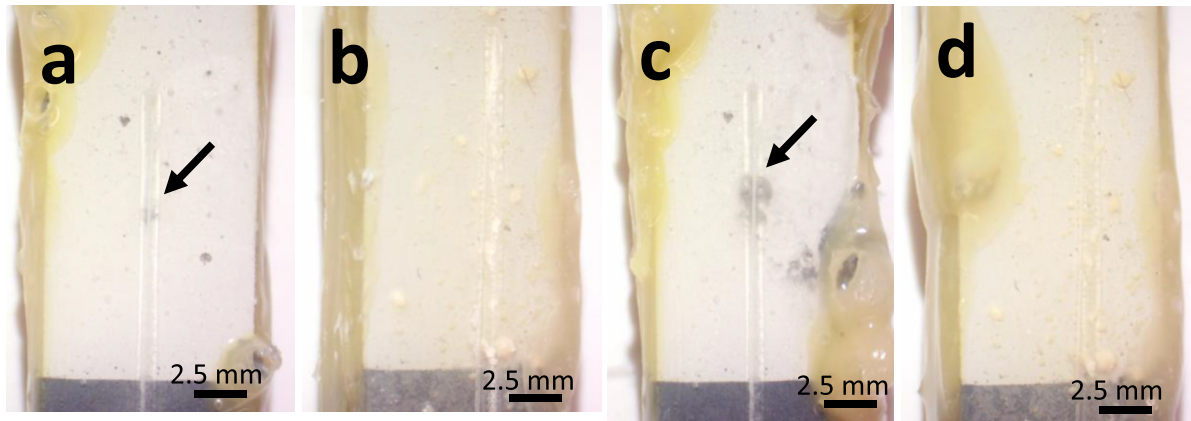


Fig. 9. Photographs of corrosion-tested FSWAZ31B alloy–titanium joints the (a) nanocontainer free and (b) with nanocontainer for 100 h immersion, (c) nanocontainer free and (d) with nanocontainer for 272 h, immersion 3.5wt% sodium chloride solution at room temperature ( $\approx 20$  °C).

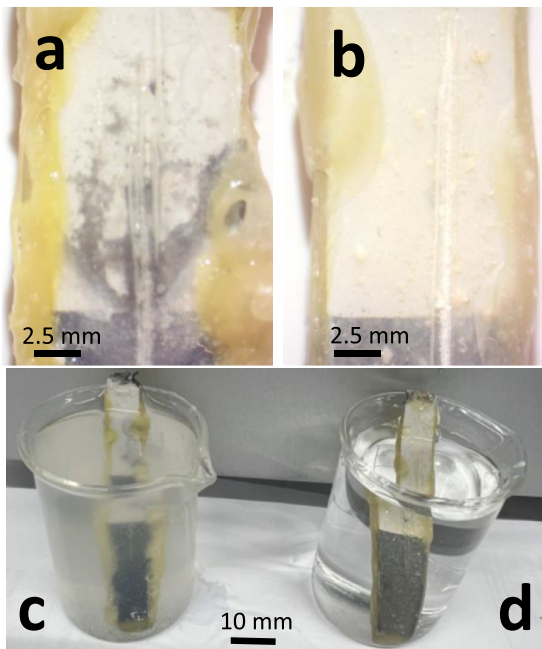


Fig. 10. Photographs of the 3.5 wt.% sodium chloride solutions following 78 h immersion of (a, c) nanocontainer free and (b, d) with nanocontainer.

scratch (Fig. 10a), whereas very minor corrosion occurred with the nanocontainer loaded epoxy (Fig. 10b) that shows the large differences in the amount of corrosion precipitation. The solution was cloudy at the end of the test of the latter specimen. After filtering and drying, 0.120 g of white precipitate ( $\text{Mg}(\text{OH})_2$ ) was collected (Fig. 10(c, d)), compared with 0.008 g for the test without nanocontainers.

The immersion test results provide valuable insights into the corrosion protection offered by the inhibitor-loaded nanocontainers in comparison to traditional coatings in a harsh 3.5 wt.% NaCl solution environment.

Firstly, the observation of a small region of corrosion on the Mg side of the scratch in the nanocontainer-free specimen after 100 h of immersion highlights the vulnerability of the unprotected substrate to corrosion. This initial corrosion area increased significantly to approximately  $1 \text{ mm}^2$  after 272 h,

indicating progressive degradation of the magnesium substrate in the absence of corrosion inhibitors.

In contrast, the specimen with an inhibitor-loaded nanocontainer epoxy coating exhibited no visible corrosion, even after prolonged immersion periods, demonstrating the effectiveness of the two-shell inhibitor in preventing corrosion initiation and propagation. This significant reduction in corrosion indicates that the inhibitor-loaded nanocontainers successfully released the inhibitor into the surrounding environment, providing continuous and sustained protection to the substrate. The limited extent of corrosion observed on the nanocontainer-free specimen after re-immersion for 78 h further emphasizes the superiority of the inhibitor-loaded nanocontainer coating in mitigating corrosion. In comparison, the specimen without nanocontainers experienced relatively severe corrosion spreading from the scratch, underscoring the critical role of the inhibitor in inhibiting corrosion progression. The cloudy appearance of the solution at the end of the test with the nanocontainer-loaded specimen suggests the formation of insoluble corrosion products, likely magnesium hydroxide ( $\text{Mg}(\text{OH})_2$ ), as a result of the inhibitor's action. The significantly higher quantity of white precipitate collected from the specimen without nanocontainers highlight the efficacy of the inhibitor-loaded nanocontainers in reducing corrosion by facilitating the formation of protective corrosion products.

#### 4. Discussion

The findings report that PEO (Plasma Electrolytic Oxidation) has a potential benefit to protect dissimilar light metal joints that are susceptible to severe galvanic corrosion [46]. The presence of a PEO coating on the welded side of the magnesium alloy serves the dual purpose of enhancing barrier protection and preventing the solution from reaching the titanium surface. This effectively diminishes the galvanic impact of titanium on the corrosion of the coated joint alloy. As shown in Fig. 8, it becomes apparent that the PEO coating's barrier properties on the Mg-Ti joint lead to an elevation in the corrosion potential when compared to the uncoated joint.

This shift is due to the restriction in the access of electrolyte from the surrounding media.

However, it is crucial to highlight that the kinetics of both the anodic and cathodic reactions show a minor improvement when compared to the uncoated joint. This observation hints at an increase in the specific surface area following the application of the PEO coating. It is noteworthy to mention that a previous report by the authors documented the extensive corrosion of the uncoated Mg-Ti joint when subjected to immersion in a 3.5 wt.% sodium chloride solution for a duration of 24 h [46]. Due to the preferential flow of electrical current towards the titanium component within the joint, coupled with differences in coating porosity and microstructure, a thicker coating, approximately 10  $\mu\text{m}$  in thickness, was formed above the titanium, whereas it measured approximately 6  $\mu\text{m}$  above the magnesium. In the absence of the PEO coating, corrosion of the bare magnesium in the joint resulted in a substantial quantity of  $\text{Mg}(\text{OH})_2$  precipitation. In contrast, corrosion of the titanium component was negligible. At the conclusion of the test, the weight of the precipitate had been reduced by a factor of approximately 8 due to the presence of the PEO coating. A significant amount of magnesium hydroxide precipitation can cause a rapid increase in the pH of the sodium chloride electrolyte, which in turn reduces the corrosion rate when compared to the PEO-coated joint. Consequently, this effect can lead to an underestimation of the corrosion reduction achieved by the coating. A further level of protection of the joint with epoxy loaded nanocontainers incorporated with inhibitors on the PEO coated joint can block the pores and limit access of the solution to the substrates. The inhibitive role of cerium ion is based on the formation of insoluble cerium hydroxide where the cathodic reaction occurs. Deposition of insoluble cerium compound can significantly reduce the cathode reaction [61]. Even intermetallic zones of the alloy can become active cathodic regions [62]. 8-HQ has hydroxyl and a tertiary amino group as an organic inhibitor. The findings are in agreement with the suggestions of Harvey et al. [63] that inhibitors with amino groups are effective inhibitors for light alloys. 8-HQ is also a cathodic inhibitor that reduces the cathodic reaction in a neutral chloride solution. However, the mechanism is based on the formation of poorly soluble chelate complexes with light alloys [64,65]. The results demonstrate that the incorporation of ceria nanocontainers (Ce@PS) loaded with 8-HQ into the PEO layer on the Mg-Ti joint improved the corrosion protective properties of the joints by increasing the corrosion potential value, presenting enhanced barrier properties and decreasing the anodic and cathodic currents compared to the PEO coatings without nanocontainers (Fig. 8). These properties can be attributed to the fact that as-received polystyrene without a crosslinking agent, which is a water-soluble-based polymer, has a stable structure in the acetonitrile [47,66]. In contrast, Ce@PS is sensitive in an aqueous environment. When damage occurs on the surface of the joint in an aqueous solution, water enters the coating, the nanocontainers starts to deform by increasing the diameter and size and changing to oval from circular [67]. In the event that a rupture emerges on the up-

per cerium oxide layer (as shown in Fig. 4), an increase in water content would lead to the widening of this defect. This expansion would facilitate the release of the organic inhibitor [23,68] and protect the joint. That is the reason that the PS polymer core was selectively and partially removed from the template.

Initially, after 100 h of immersion, a small region of corrosion was observed on the Mg side of the scratch in the specimen without nanocontainers, while no corrosion was evident on the specimen with nanocontainers. This behaviour suggests that the presence of inhibitor-loaded nanocontainers effectively inhibited corrosion initiation and propagation, thus preserving the integrity of the coated surface. As the immersion period extended to 272 h, the extent of corrosion on the nanocontainer-free specimen increased significantly, reaching approximately 1  $\text{mm}^2$ . In contrast, the specimen with nanocontainers continued to exhibit minimal corrosion, indicating sustained protection over an extended period. This difference in corrosion behaviour underscores the long-term efficacy of the inhibitor-loaded nanocontainers in preventing corrosion progression. Upon re-scratching and re-immersing the specimens for an additional 78 h, the corrosion observed on the nanocontainer-free specimen became more severe, with corrosion spreading from the scratch. In contrast, the specimen with nanocontainers continued to display minimal corrosion, further demonstrating the superior corrosion resistance conferred by the inhibitor-loaded nanocontainers.

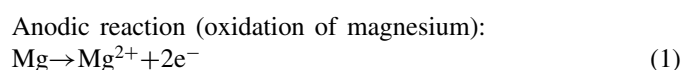
#### 4.1. Mechanism of corrosion protection using two-shell nanocontainers

PEO coatings primarily offer barrier protection, which is heavily reliant on the integrity of the thin oxide layer, typically  $<1 \mu\text{m}$  thick, as a barrier coating. This oxide layer acts as the main protection against corrosion. The porous outer layer of the coating can also contribute to corrosion protection by slowing the transport of corrosive species between the substrate and the surrounding environment. However, if the barrier layer in a coating on magnesium is weakened, often due to the presence of defects, corrosive solutions can penetrate the coating, leading to the initiation of corrosion.

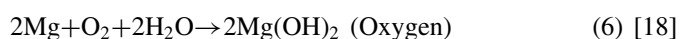
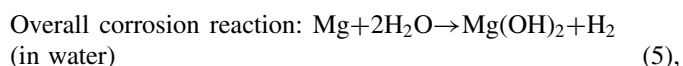
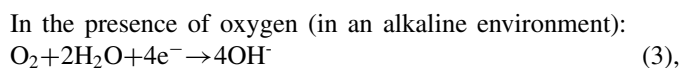
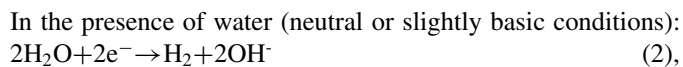
Beyond protecting the AZ31B alloy, the PEO coating on a welded joint serves an additional function by preventing corrosive solutions from reaching the titanium surface. This effectively minimizes the galvanic interaction between titanium and the coated magnesium alloy, thereby reducing the likelihood of corrosion. To further enhance the protection of such joints, an additional layer of protection, including two types of inhibitors as a nanocontainer, was introduced.

##### 4.1.1. Corrosion reactions in magnesium

The general formula for the corrosion of magnesium in an aqueous environment (such as water or humid air) can be represented by the chemical reactions:



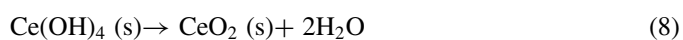
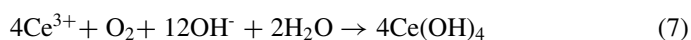
There are a couple of possible cathodic reactions depending on the environment for reduction of water/ oxygen on the metal surface by simultaneous oxidation of metal:



The two-shell nanocontainers are designed to enhance corrosion protection by utilizing a dual-inhibitor system. The outer shell, composed of cerium, and the inner core, containing 8-hydroxyquinoline (8-HQ), work together to provide both immediate and sustained corrosion inhibition.

#### 4.1.2. The protective mechanism of cerium

Upon coating damage or exposure to corrosive environments, cerium migrates towards the cathodic sites to hinder the cathodic reaction, which is enhanced by the formation of protective oxide layers. The presence of oxygen causes  $\text{Ce}^{3+}$  to oxidise to  $\text{Ce}^{4+}$  then precipitate in the presence of hydroxide to form insoluble cerium hydroxide or oxide when the pH rises near the zone of damage [69]. This blocks the cathodic sites and blocks further reduction by oxygen [70,71].



$\text{O}_2$  acts as the oxidant agent and  $\text{Ce}^{3+}$  as the reductant while  $\text{OH}^-$  ions required for the above reactions are generated by  $\text{O}_2$  driven by anodic dissolution of the metal. The cerium component of the outer shell of the nanocontainer offers protective benefits through its ability to form stable, passive films on the metal surface. These films act as a physical and chemical barrier against corrosive elements, thereby reducing the overall corrosion rate.

#### 4.1.3. The inhibition mechanism of 8-Hydroxyquinoline

The polystyrene core of the nanocontainer serves as a reservoir for the 8-HQ inhibitor. Upon coating damage, the polystyrene is gradually degraded or dissolved, leading to the controlled release of 8-HQ. This ensures that the inhibitor is available to neutralize corrosive agents over time. The inhibition activity of 8-HQ is related to the formation of insoluble chelate compounds with metal ions (Ti, Mg), which

physically block the active corrosion sites [72]. The remaining 8-HQ is adsorbed on the metallic surface, hindering the access of detrimental  $\text{Cl}^-$  ions, providing further protection [73]. Therefore the outer cerium layer acts as a barrier to initial corrosive attacks, while the inner 8-HQ is gradually released to counteract ongoing corrosion. The combination of cerium and 8-HQ provides a synergistic effect, where cerium enhances the formation of protective oxide layers, and 8-HQ interferes with the corrosion process by chelating with metal ions or neutralizing aggressive anions. This dual inhibition mechanism is particularly effective in dissimilar metal joints where corrosion can be exacerbated by galvanic interactions. This dual action provides both immediate and long-term protection. These results highlight the importance of the encapsulation of the corrosion inhibitors to prevent its oxidation and to promote its precipitation on the active corrosion sites. The approach is particularly beneficial for Ti-Mg dissimilar joints, which are prone to galvanic corrosion due to the different electrochemical potentials of titanium and magnesium. The nanocontainers help mitigate this issue by providing localized and sustained protection. This technology has significant implications for industries such as aerospace and automotive, where lightweight Ti-Mg alloys are used extensively.

## 5. Conclusion

- The study successfully demonstrates the formation and characterization of two shell Ce@PS nanocontainers loaded with 8-hydroxyquinoline (8-HQ) for corrosion protection purposes. The process involves several stages, including the creation of an outer layer of cerium around polystyrene nanospheres, selective removal of the polystyrene template to create a porous structure, loading of the 8-HQ corrosion inhibitor.
- Structural and compositional analysis using STEM observations and EDS mapping confirmed the successful loading of 8-HQ into the nanocontainers. The FTIR spectra provided insights into the chemical composition of the materials at different stages of synthesis, confirming the presence of polystyrene, cerium components, and the loaded inhibitor. The two-shell thickness is limited by polystyrene diameter to  $\sim 450$  nm which are cerium-rich in the outer region and organic-rich in the inner region.
- Thermal decomposition analysis revealed the stability of the synthesized materials under increasing temperatures, with residue remaining after decomposition indicating the presence of the cerium component.
- The corrosion evaluation of Ti-Mg joints treated with PEO coatings and loaded nanocontainers demonstrated improved corrosion resistance compared to bare joints. Potentiodynamic polarization curves revealed an increase in corrosion potential and a decrease in corrosion current density for joints with loaded nanocontainers, indicating enhanced corrosion protection.



## Declaration of competing interest

The authors declare that they have no known competing financial interests or personal relationships that could have appeared to influence the work reported in this paper.

## CRedit authorship contribution statement

**Sepideh Aliasghari:** Writing – review & editing, Writing – original draft, Supervision, Methodology, Investigation, Funding acquisition, Formal analysis, Conceptualization. **Teruo Hashimoto:** Formal analysis. **Peter Kelly:** Writing – review & editing. **Allan Matthews:** Writing – review & editing.

## Acknowledgements

The authors would like to express their deep gratitude to Professor Peter Skeldon for his invaluable comments and insights. His expertise and thoughtful feedback significantly contributed to the improvement of this work.

## Supplementary materials

Supplementary material associated with this article can be found, in the online version, at [doi:10.1016/j.jma.2024.09.004](https://doi.org/10.1016/j.jma.2024.09.004).

## References

- [1] M. Aonuma, K. Nakata, *Mater. Sci. Eng.: B* 177 (2012) 543–548.
- [2] M. Aonuma, K. Nakata, *Mater. Sci. Eng.: B* 161 (2009) 46–49.
- [3] S. Madhavan, M. Kamaraj, L. Vijayaraghavan, K.Srinivasa Rao, *Trans. Indian Inst. Metals* 70 (2017) 1047–1054.
- [4] S. Aliasghari, P. Skeldon, G. Thompson, *Appl. Surf. Sci.* 316 (2014) 463–476.
- [5] J. Curran, H. Kalkanci, Y. Magurova, T. Clyne, *Surf. Coat. Technol.* 201 (2007) 8683–8687.
- [6] M. Shokouhfar, C. Dehghanian, M. Montazeri, A. Baradaran, *Appl. Surf. Sci.* 258 (2012) 2416–2423.
- [7] P. Huang, K.-W. Xu, Y. Han, *Mater. Lett.* 59 (2005) 185–189.
- [8] X. Zhang, S. Aliasghari, A. Nemcova, T.L. Burnett, I. Kubena, M. Smid, G.E. Thompson, P. Skeldon, P.J. Withers, *ACS Appl. Mater. Interfaces* 8 (2016) 8801–8810.
- [9] C. Dunleavy, J. Curran, T. Clyne, *Appl. Surf. Sci.* 268 (2013) 397–409.
- [10] Z. Li, X. Jing, Y. Yuan, M. Zhang, *Corros. Sci.* 63 (2012) 358–366.
- [11] R. Arrabal, J. Mota, A. Criado, A. Pardo, M. Mohedano, E. Matykina, *Surf. Coat. Technol.* 206 (2012) 4692–4703.
- [12] A. Gnedenkov, S. Sinebryukhov, D. Mashtalyar, S. Gnedenkov, *Corros. Sci.* 102 (2016) 348–354.
- [13] A. Gnedenkov, S. Sinebryukhov, D. Mashtalyar, S. Gnedenkov, *Corros. Sci.* 102 (2016) 269–278.
- [14] M. Mohedano, M. Serdechnova, M. Starykevich, S. Karpushenkov, A. Bouali, M. Ferreira, M. Zheludkevich, *Mater. Des.* 120 (2017) 36–46.
- [15] G. Zhang, L. Wu, A. Tang, Y. Ma, G.-L. Song, D. Zheng, B. Jiang, A. Atrens, F. Pan, *Corros. Sci.* 139 (2018) 370–382.
- [16] D. Jiang, X. Xia, J. Hou, G. Cai, X. Zhang, Z. Dong, *Chem. Eng. J.* 373 (2019) 285–297.
- [17] B. Mingo, Y. Guo, R. Leiva-Garcia, B.J. Connolly, A. Matthews, A. Yerokhin, *ACS Appl. Mater. Interfaces* 12 (2020) 30833–30846.
- [18] S. Al Abri, A. Rogov, S. Aliasghari, A. Bendo, A. Matthews, A. Yerokhin, B. Mingo, *J. Mater. Res. Technol.* 30 (2024) 2365–2376.
- [19] I. Cole, *Handbook of Smart Coatings for Materials Protection*, 2014, pp. 29–55. DOI.
- [20] M. Zheludkevich, J. Tedim, M. Ferreira, *Electrochim. Acta* 82 (2012) 314–323.
- [21] R.S. Jadhav, D.G. Hundiwale, P.P. Mahulikar, *J. Appl. Polym. Sci.* 119 (2011) 2911–2916.
- [22] U.S. Chung, J.H. Min, P.-C. Lee, W.-G. Koh, *Colloids Surf. A: Physicochem. Eng. Aspects* 518 (2017) 173–180.
- [23] A. Balaskas, T. Hashimoto, M. Curioni, G. Thompson, *Nanoscale* 9 (2017) 5499–5508.
- [24] V. Nardello-Rataj, L. Leclercq, Beilstein. *J. Org. Chem.* 10 (2014) 2603–2622.
- [25] X.-M. Tong, T. Zhang, M.-Z. Yang, Q. Zhang, *Colloids Surf. A: Physicochem. Eng. Aspects* 371 (2010) 91–97.
- [26] G. Wu, J. An, X.Z. Tang, Y. Xiang, J. Yang, *Adv. Funct. Mater.* 24 (2014) 6751–6761.
- [27] H. Li, Y. Cui, H. Wang, Y. Zhu, B. Wang, *Colloids Surf. A: Physicochem. Eng. Aspects* 518 (2017) 181–187.
- [28] M. Samadzadeh, S.H. Boura, M. Peikari, S. Kasirha, A. Ashrafi, *Prog. Org. Coat.* 68 (2010) 159–164.
- [29] T. Judit, S. Abdul, V. Gyöngyi, in: *Micro/Nanocapsules for Anticorrosion Coatings, Fundamentals of Nanoparticles*, Elsevier, 2018, pp. 521–551.
- [30] V.V. Gite, P.D. Tatiya, R.J. Marathe, P.P. Mahulikar, D.G. Hundiwale, *Prog. Org. Coat.* 83 (2015) 11–18.
- [31] R.J. Marathe, A.B. Chaudhari, R.K. Hedaoo, D. Sohn, V.R. Chaudhari, V.V. Gite, *RSC Adv.* 5 (2015) 15539–15546.
- [32] M. Okubo, H. Minami, Y. Jing, *J. Appl. Polym. Sci.* 89 (2003) 706–710.
- [33] D.G. Shchukin, M. Zheludkevich, K. Yasakau, S. Lamaka, M.G. Ferreira, H. Möhwald, *Adv. Mater.* 18 (2006) 1672–1678.
- [34] C. Ding, Y. Liu, M. Wang, T. Wang, J. Fu, *J. Mater. Chem. A* 4 (2016) 8041–8052.
- [35] M. Yeganeh, M. Omid, S. Mortazavi, A. Etemad, M. Nazari, S. Marashi, in: *Application of Mesoporous Silica as the Nanocontainer of Corrosion Inhibitor, Corrosion Protection at the Nanoscale*, Elsevier, 2020, pp. 275–294.
- [36] S. Sonawane, B. Bhanvase, A. Jamali, S. Dubey, S. Kale, D. Pinjari, R. Kulkarni, P. Gogate, A. Pandit, *Chem. Eng. J.* 189 (2012) 464–472.
- [37] M. Montemor, D. Snihirova, M. Taryba, S. Lamaka, I. Kartsonakis, A. Balaskas, G. Kordas, J. Tedim, A. Kuznetsova, M. Zheludkevich, *Electrochim. Acta* 60 (2012) 31–40.
- [38] A. Balaskas, I. Kartsonakis, L.-A. Tziveleka, G. Kordas, *Prog. Org. Coat.* 74 (2012) 418–426.
- [39] G.L. Li, M. Schenderlein, Y. Men, H. Möhwald, D.G. Shchukin, *Adv. Mater. Interfaces* 1 (2014) 1300019.
- [40] J.D. Rule, N.R. Sottos, S.R. White, *Polymer* 48 (2007) 3520–3529.
- [41] A.S.H. Makhlof, *Handbook of Smart Coatings for Materials Protection*, Elsevier, 2014.
- [42] T. Szabó, L. Molnár-Nagy, J. Bognár, L. Nyikos, J. Telegdi, *Prog. Org. Coat.* 72 (2011) 52–57.
- [43] E.N. Brown, S.R. White, N.R. Sottos, *J. Mater. Sci.* 39 (2004) 1703–1710.
- [44] A. Baron-Wiecheć, M. Curioni, R. Arrabal, E. Matykina, P. Skeldon, G. Thompson, *Trans. IMF* 91 (2013) 107–112.
- [45] G. Alisch, D. Nickel, T. Lampke, *Surf. Coat. Technol.* 206 (2011) 1085–1090.
- [46] S. Aliasghari, A. Rogov, P. Skeldon, X. Zhou, A. Yerokhin, A. Aliabadi, M. Ghorbani, *Surf. Coat. Technol.* 393 (2020) 125838.
- [47] P. Bilalis, E.K. Efthimiadou, A. Chatzipavlidis, N. Boukos, G.C. Kordas, *Polym. Int.* 61 (2012) 888–894.
- [48] N. Manikandan, *Int. J. Recent Innov. Trends Comput. Commun* 2 (2014) 1148–1151.
- [49] S. Lias, J. Bartmess, J. Liebman, J. Holmes, R. Levin, G. Mallard, in: *NIST Chemistry Webbook Standard Reference Database Number 69*, National Institute of Standards Technology, 2010, p. 1.
- [50] I.A. Kartsonakis, G. Kordas, *J. Am. Ceram. Soc.* 93 (2010) 65–73.
- [51] T. Ristoiu, L. Ciontea, T. Petrisor Jr, M. Gabor, T. Petrisor, *Studia Universitatis Babeş-Bolyai, Chemia* 56 (2011).
- [52] I. Zagaynov, S. Kutsev, *Appl. Nanosci.* 4 (2014) 339–345.

- [53] W.C. Andersen, B.C. Noll, S.P. Sellers, L.L. Whildin, R.E. Sievers, *Inorganica Chim. Acta* 336 (2002) 105–110.
- [54] H. Hang, R.M. Altarawneh, T.M. Brueckner, P.G. Pickup, *J. Electrochem. Soc.* 167 (2020) 054518.
- [55] E. Matykina, R. Arrabal, P. Skeldon, G. Thompson, *Acta Biomater.* 5 (2009) 1356–1366.
- [56] A. Bordbar-Khiabani, B. Yarmand, M. Mozafari, *Mater. Lett.* 258 (2020) 126779.
- [57] F. Bai, H. Su, F. Chang, *Chem. Lett.* 36 (2007) 1104–1105.
- [58] N. Van Phuong, B.R. Fazal, S. Moon, *Surf. Coat. Technol.* 309 (2017) 86–95.
- [59] R. Arrabal, E. Matykina, T. Hashimoto, P. Skeldon, G. Thompson, *Surf. Coat. Technol.* 203 (2009) 2207–2220.
- [60] S. Morsch, S. Lyon, P. Greensmith, S. Smith, S. Gibbon, *Faraday Discuss.* 180 (2015) 527–542.
- [61] K. Yasakau, M. Zheludkevich, O. Karavai, M. Ferreira, *Prog. Org. Coat.* 63 (2008) 352–361.
- [62] V. Palanivel, Y. Huang, W.J. van Ooij, *Prog. Org. Coat.* 53 (2005) 153–168.
- [63] T. Harvey, S. Hardin, A. Hughes, T. Muster, P. White, T. Markley, P. Corrigan, J. Mardel, S. Garcia, *J. Mol. Corros. Sci.* 53 (2011) 2184–2190.
- [64] S.V. Lamaka, M.L. Zheludkevich, K. Yasakau, M. Montemor, M.G. Ferreira, *Electrochim. Acta* 52 (2007) 7231–7247.
- [65] E.D. Mekeridis, I.A. Kartsonakis, G.C. Kordas, *Prog. Org. Coat.* 73 (2012) 142–148.
- [66] I.A. Kartsonakis, A.C. Balaskas, G.C. Kordas, *Corros. Sci.* 53 (2011) 3771–3779.
- [67] I. Kartsonakis, E. Koumoulos, A. Balaskas, G. Pappas, C. Charitidis, G. Kordas, *Corros. Sci.* 57 (2012) 56–66.
- [68] A.C. Balaskas, M. Curioni, G.E. Thompson, *Surf. Interface Anal.* 47 (2015) 1029–1039.
- [69] F. Scholes, C. Soste, A. Hughes, S. Hardin, P. Curtis, *Appl. Surf. Sci.* 253 (2006) 1770–1780.
- [70] S.A. Hayes, P. Yu, T.J. O’Keefe, M.J. O’Keefe, J.O. Stoffer, *J. Electrochem. Soc.* 149 (2002) C623.
- [71] A. Hughes, J. Gorman, P. Miller, B. Sexton, P. Paterson, R. Taylor, *Surf. Interface Anal.: Int. J. Devoted Dev. Appl. Tech. Anal. Surf., Interfaces Thin Films* 36 (2004) 290–303.
- [72] M.J. Anjum, J. Zhao, V.Z. Asl, G. Yasin, W. Wang, S. Wei, Z. Zhao, W.Q. Khan, *Corros. Sci.* 157 (2019) 1–10.
- [73] A. Galio, S. Lamaka, M. Zheludkevich, L. Dick, I. Müller, M. Ferreira, *Surf. Coat. Technol.* 204 (2010) 1479–1486.